Effect of perovskite absorber thickness and working temperature on the hematite-based ETL in PSCs

Prajwal Reddy Korem[1], *Manpreet* Kaur[2], *Manisha* Kumari[3], and *Ankush* Kumar Tangra[4*]

[1] University of North Texas, Department of Data Analytics & Statistics, Denton, USA
[2]Arya Model Senior Secondary School, Department of Physics, Phagwara, Punjab, India
[3]DAV University, Department of Physics, Jalandhar, Punjab, India
[4]Department of Physics, Bahra Research Innovation & Knowledge Cluster, University School of Sciences, Rayat Bahra University, Greater Mohali, Punjab, 140103, India

Abstract. A key factor in increasing the efficiency of perovskite solar cell (PCSs) is optimizing the thickness of the absorber and the operating temperature. In order to examine the impact of these factors, a planar *n-i-p* PSCs with the configuration FTO/α-Fe_2O_3/$MAPbI_3$/Spiro-OMeTAD/Au was simulated using SCAPS-1D. The results indicate that the charge carrier generation and transportation are strongly governed by the thickness of $MAPbI_3$ absorber layer. When tune to 600 nm thickness, the device has a Jsc of 22.1 mA/cm^2, an Voc of 1.06 V, a FF of 77.4 %, and an overall PCE of 18.3 %. When layers are too thin (<300 nm), they limit the photon absorption, which lower the Jsc. When layers are too thick (>800nm), they cause recombination losses that lower the FF. Variation in the temperature also affect how well the device works in different temperature conditions. For example, raising form 300 K to 350 K lowers the Voc and PCE because of non-radiative recombination happens more often. These finding highlight that careful control of absorber thickness coupled with thermal stability of the α-Fe_2O_3 ETL is crucial for achieving stable and high-efficiency PSCs.

1 Introduction

Research on next-generation photovoltaic technologies has increased due to the growing demand for sustainable and clean energy on the global scale. PSCs shows the promising approach for the clean energy due to its unique properties viz. low-cost, manufacturing costs, higher optoelectronic characteristics, and rapidly rising power conversion efficiencies (PCE). After making impressive strides in less than 10 years, PSCs have quickly become traditional photovoltaic systems. By 2023, their PCE has increased from the initial reports in 2009 to 27 %, highlighted their remarkable potential for next generation solar energy technologies [1-3]. As an alternative to traditional solar cells, perovskite materials are known for their efficiency and low cost. The architecture of PSCs generally consist of five functional layers: TCO, ETL, Perovskite absorber layer (PAL), HTL and gold (Au) back contact layer make up a typical planar n-i-p configuration structure [4]. Rahman et al. in 2019, reported that these

* Corresponding author: aktangra@gmail.com

layers effectively reduced the electron recombination and promotes hole extraction from the PAL [4]. The PAL in PSCs which oblige as the main photon harvesting material is crucial to the overall functionality of the solar device. Extensive literature reveals that the thickness of PAL strongly impact the efficiency of the PSCs. Similarly, the thickness of ETL/HTL also play a crucial role in the device performance [5-10]. Hematite (α-Fe_2O_3), an n-type semiconductor, has increased noteworthy attention in PV industry owing to its outstanding stability, cheap material cost, and encouraging band alignment [11]. The operational extraction and transfer of electrons from the PAL to the cathode is made possible by α-Fe_2O_3 with the energy band gap of about ~2.1 eV and its ideally situated conduction band [12-14]. α-Fe_2O_3 is considered a very favourable material for the ETL in PSCs because of its excessive UV stability and proficient absorption in the visible region. Furthermore, α- Fe_2O_3 thin films show a transparency of about 70-85 % within the 600-1000 nm wavelength range, confirming good optical transparency across the visible region [15]. α-Fe_2O_3 is also readily available in nature and inexpensive to manufacture. Its advantageous electrical properties make it possible for photogenerated electrons to be transferred to the electrode efficiently, thereby enhancing the current generation in solar cell applications. A comparison table of the inorganic ETL based PSCs as presented in Table 1.

Table 1. Signifies the comparable analysis of the inorganic ETL base PSCs.

Device	VOC (V)	JSC (mA/cm²)	FF (%)	PCE (%)	Ref.
ITO/ZnO/MAPbI3/spiro-OMeTAD/Ag	1.03	20.4	75	15.7	13
FTO/SnO_2/$MAPbI_3$/spiro-OMeTAD/Au	1.11	23.3	67	17.2	
FTO/SnS_2/$MAPbI_3$/spiro-OMeTAD/Au	0.95	23.7	60	13.6	
FTO/TiO_2 coated WO_3/$MAPbI_3$/spiro-OMeTAD/A	0.87	17.0	76	11.2	
ITO/CdS/perovskite/spiro-OMeTAD/Au	1.05	16.14	66	11.2	
FTO/α-Fe_2O_3/$MAPbI_3$/Spiro-OMeTAD/Au (Theo.)	1.06	22.1	77	18.3	

In this work, our aim is dedicated on influence the thickness of PAL and operating temperature on the solar cell using SCAPS-1D. A standard *n-i-p* device design of FTO/α-Fe_2O_3/$MAPbI_3$/Spiro-OMeTAD/Au was engaged. Additionally, influence of changing temperatures from (250 K to 350 K) on key solar cell parameters includes FF (Fill factor), V_{OC} (Voltage), J_{SC} (short-circuit current density), and PCE was systematically analyzed and examined in depth.

2 Device simulation

SCAPS-1D, is broadly used as a simulator tool for solar cell simulation, which is developed at the Ghent University, Department of Electronics, was employed to simulate the performance of the proposed PSCs. With its ability to accurately predict the electro-optical behaviour of heterojunction and multilayer thin film solar device. The program uses light to numerically solve a series of basic equations, such as Poisson's equation and the charge carrier continuity equations. This simulation tool offers comprehensive insights into how

device materials parameters, interfacial features, and layer thickness affect device performance by taking into consideration the internal electrostatic potential, quasi Fermi level splitting, and the spatial distribution of charge carrier densities. This computational outline enables a systematic evaluation of design selections, allowing optimisation prior to experimental synthesis. In this our work, we simulated a *n-i-p* configuration solar device, with structured as FTO/α-Fe_2O_3/$MAPbI_3$/Spiro-OMeTAD/Au as revealed in Figure 1. The diagram architecture of the fabricated PSCs, comprising a transparent FTO substrate, α-Fe_2O_3 as the ETLs, $CH_3NH_3PbI_3$ as the PAL, Spiro-OMeTAD as the HTLs, and top electrode is Au.

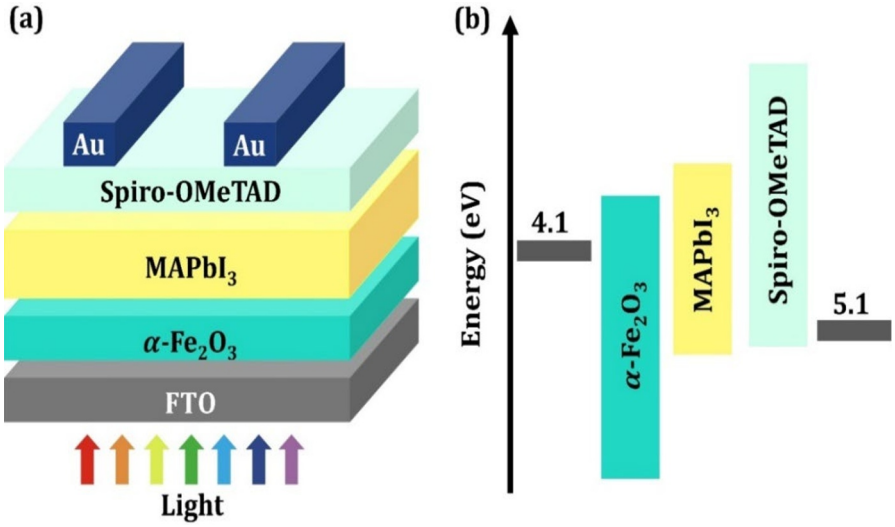

Fig. 1. (a) Represents the simulated device FTO/*α*-Fe_2O_3/$MAPbI_3$/Spiro-OMeTAD/Au solar cell, and (b) Energy level diagram presenting band alignment for effective charge transfer.

Table 2. Conduction and valence band position of α-Fe_2O_3, $MAPbI_3$, and Spiro-OMeTAD.

Materials	CBM	VBM
α-Fe_2O_3	~4.1	~7.40
$MAPbI_3$	~3.90	~5.43
Spiro-OMeTAD	~2.20	~5.1

The configuration enables efficient absorption of incident light within the PAL, while α-Fe_2O_3 and Spiro-OMeTAD facilitate selective charge extraction and transport toward the electrodes. The parallel energy band alignment is presented in Figure 1 (b). The conduction band position of α-Fe_2O_3 (4.1 eV) aligns favourably with the $MAPbI_3$ perovskite, enabling efficient electron injection and transport while minimising energy losses. In comparsion, the valence band of $CH_3NH_3PbI_3$ couples effectively with HTL (5.1 eV), promoting rapid hole extraction and hindered the recombination at the device interfaces. By providing a matched energy bands ensures directional electron/holes flow towards the tansport layers, thereby enhancing both charge separation efficiency and overall solar device performance. The combined effects of layers and aligned bands supports the increase in the efficiency and stability of device. The corresponding energy levels and interfacial band offsets are brief in table 2.

3 Discussion

The energy band diagram of the designed *n-i-p* PSCs is represented in Figure 2. The conduction (E_c) and valence band (E_p) are shown as a vertical device position, quasi-Fermi level for electrons (E_{Fc}) and for holes (E_{Fp}) indicate the splitting of carrier populations under radiance.

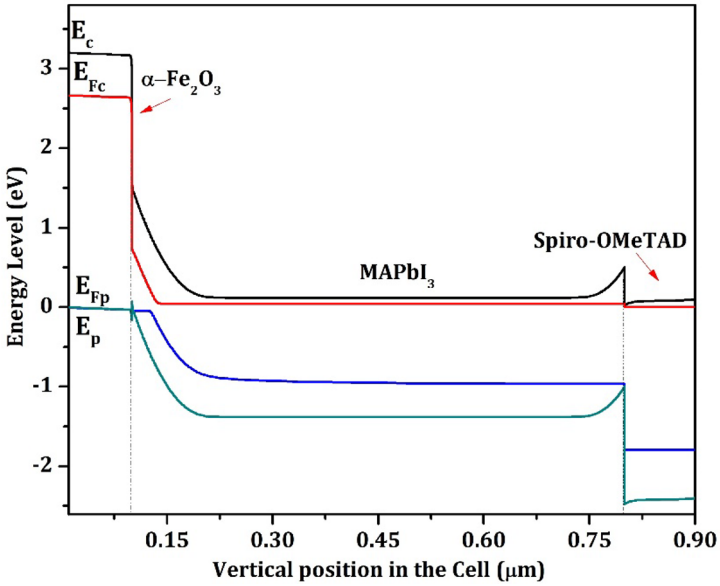

Fig. 2. Represents the bands alignment of the different PSCs layers.

The E_c of α-Fe_2O_3 aligns satisfactorily with $CH_3NH_3PbI_3$, supporting directed efficient electron transport while preventing unwanted holes backflow. Within the PAL, the separation of E_{Fc} and E_{Fp} reflects strong photo-generation and charge carrier dynamics. Toward the back contact, the E_p of Spiro-OMeTAD provide an energetically well-matched pathway for hole extraction while simultaneously blocking electron leakage. By establishing a better bands alignments will ensure directional electron/holes separation, minimises interfacial recombination, and contributes directly to the high Voc and overall device PCE of the solar cell. Table 3 encapsulates the materials and simulation parameters engaged for the FTO/α-Fe_2O_3/$MAPbI_3$/Spiro-OMeTAD/Au device architecture. Figure 3 presents the quantum efficiency (QE) spectrum along with the J-V characteristics. Figure 3 (a) displays the J-V behaviour of the FTO/α-Fe_2O_3/$MAPbI_3$/Spiro-OMeTAD/Au device under illumination. The device delivers a V_{OC} of ~1.06 V, a J_{SC} of ~22.17 $mAcm^{-2}$, an FF of ~ 77.38% and a PCE of ~18.31 %. The relatively high Jsc arises from the excellent high harvesting ability of the $MAPbI_3$ absorber, which efficiently captures photons in the visible region and generates a large number of charge carriers. The superior fill factor indicates a reduction series resistance and demonstrates efficient charge transport across the α-Fe_2O_3/$MAPbI_3$ and $MAPbI_3$/Spiro-OMeTAD interfaces. This suggests that recombination losses are minimized and that the energy band alignment has been optimised effectively. The high fill factor results from efficient charge extraction and minimal internal resistance, as evidenced by the distinct knee of the curve near the point of optimal power generation.

Table 3. Materials properties and simulation parameters for the FTO/α-Fe_2O_3/$MAPbI_3$/Spiro-OMeTAD/Au perovskite solar cell architecture.

Parameters (*)	α-Fe_2O_3	$MAPbI_3$	Spiro-OMeTAD
A	0.100	0.600	0.100
B	2.500	1.500	3.200
C	4.000	3.520	2.050
D	10.000	4.200	4.500
E	2.000E+18	1.000E+18	2.200E+18
F	1.800E+19	1.000E+18	1.800E+19
G	1.000E+7	1.000E+7	1.000E+7
H	1.000E+7	1.000E+7	1.000E+7
I	2.000E+5	2.200E+3	2.000E-6
J	1.000E+5	2.200E+3	2.000E-6

** A = Thickness (μm), B = Band gap (eV) C = Electron affinity (eV) D = Dielectric Permittivity (relative) E = CB effective density of states (cm^{-3}) F = VB effective density of states (cm^{-3}) G = Electron thermal velocity ($cm\ s^{-1}$) H = Hole thermal velocity ($cm\ s^{-1}$) I = Electron mobility ($cm^2V^{-1}s^{-1}$) J = Hole mobility ($cm^2V^{-1}s^{-1}$).*

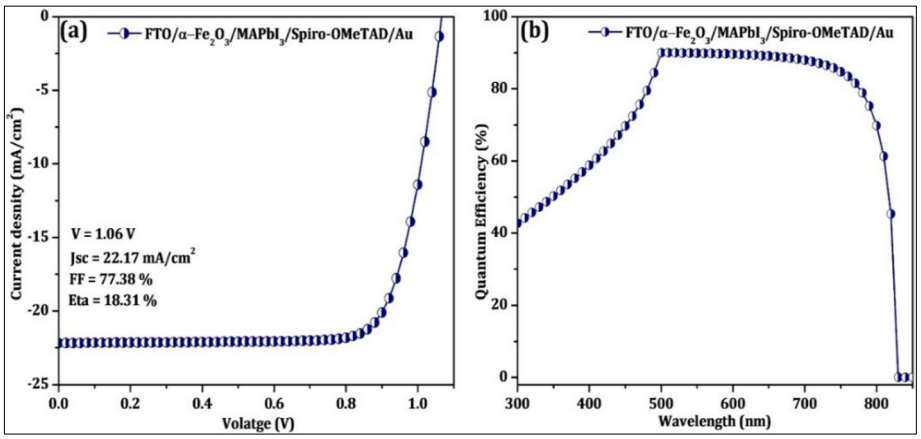

Fig. 3. (a) JV characteristics of the stimulated solar device, and (b) Quantum Efficiency curve.

These results indicate that the device efficiently converts incoming photons into usable electrical energy. Furthermore, Figure 3 (b) shows the QE spectrum of the device. The QE is approximately 90 % in the 500-750 nm range, confirming that the $MAPbI_3$ absorber layer contributes significantly to photocurrent generation across the visible spectrum. This broad and high QE response explains the elevated Jsc observed in J-V curve. Thus, the photon absorption of PAL, combined with high FF resulting efficient charge extraction, underpins the excellent solar cell device performance. Figure 4. proves the JV characteristics of the FTO/α-Fe_2O_3/$MAPbI_3$/Spiro-OMeTAD/Au device structure measured at different PAL

thickness, ranging from 200 nm to 900 nm. The curves demonstrate how the thickness of the PAL significantly influences the PV response.

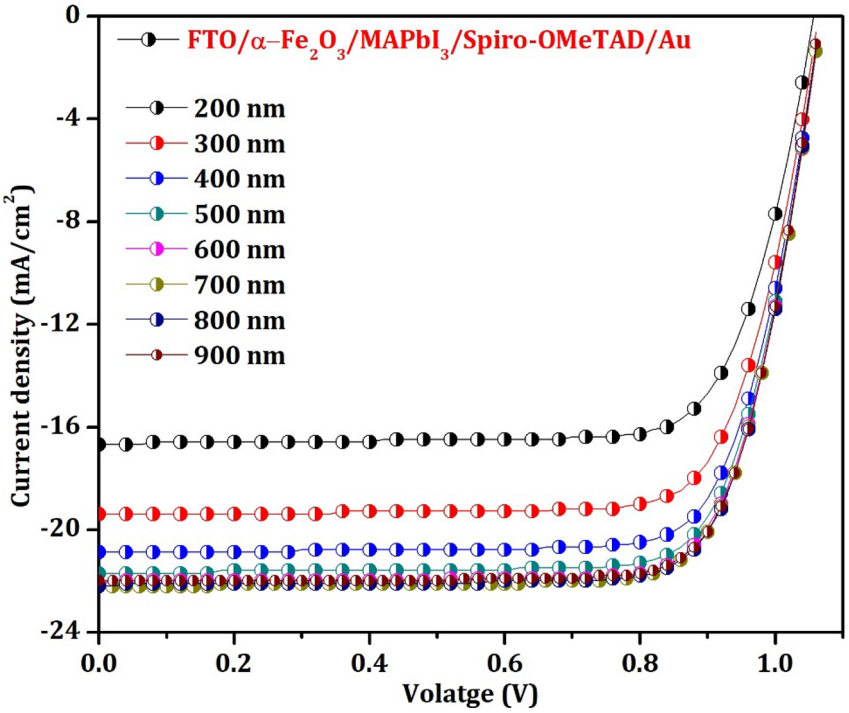

Fig. 4. Variation in JV characteristics of the stimulated solar device under different absorber thickness (200-900 nm).

At 200-300 nm thickness, the JV curve is relatively low, which can be attributed to inadequate light absorption and reduced photo-generated carrier density. As the thickness increases (400-700 nm), both the Jsc and overall device performance is enhanced due to enhanced in photon harvesting and more efficient charge generation. However, beyond an optimal thickness, such as at 800-900 nm, a decline in current density is observed. This reduction may result from increased carrier recombination and limited charge transport through the thicker perovskite layer. Overall, the IV curves confirm the role of PAL thickness in determining the equilibrium between photon absorption and electron hole carrier collection efficiency. Optimising this parameter is essential to maximize the PCE of the PSCs.

Figure 5 illustrates the basic of PV parameters on the PAL thickness. As revealed in Figure 5 (a), both the FF and PCE exhibit a positive correspondence with thickness up to 500 nm, beyond which the values tend to saturate.

The FF maintaining a value near to ~77.54 %, whereas the efficiency reaches an extreme of ~18.31 %. This enhanced performance is attributed due to high optical absorption at high thickness, which allows for more efficient photo generation of charge carriers. But, the optimum thickness, carrier recombination and transport resistance limit further improvements in solar device performance. Also, Figure 5 (b) establishes that the Voc increases slightly with thickness before levelling off near ~1.066 V, while the Jsc shows a prominent improvement up to 700 nm (22.17 mA/cm^2). After surpassing this thickness, the PCE has no longer improves, signifying that the saturation of the photon harvesting and recombination losses begin to limit further efficiency gains. These results confirm that PAL thickness plays a decisive role in optimising solar cell performance, where ~ 500-600 nm provides the unsurpassed balance between photon absorption, electron/hole transport, and hindered recombination.

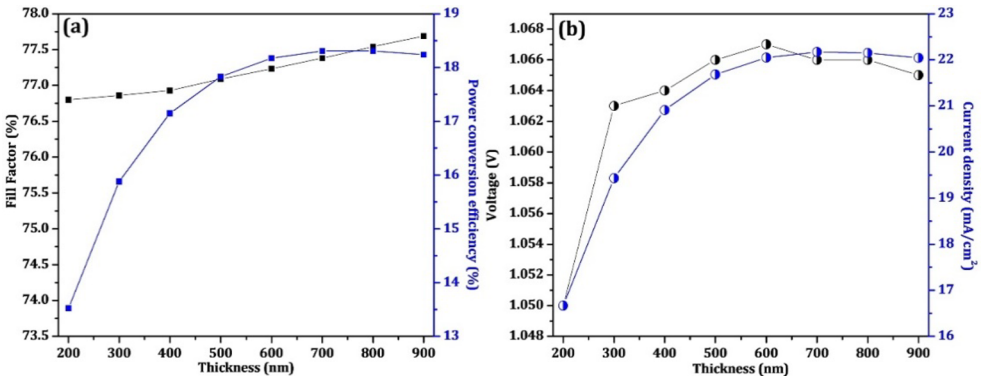

Fig. 5. Shows thickness-dependent evolution of photovoltaic parameters (PCE, FF, Voc, and Jsc), on device performance.

Figure 6 (a) represents the dependence of Voc and Jsc on working temperature. A notable inverse relationship is obtained between Voc and Jsc, Voc is decreased as the temperature increased, whereas Jsc exhibits a slight increase as the temperature increased till 350 K. the decrease in the Voc is due to from enhanced non-radiative recombination as the temperature increased, which narrows the quasi-fermi level splitting. Additionally, the reason behind the increased in the Jsc is due to increased in the charge carrier mobility and enhanced photo generation efficiency. Moreover, Figure 6 (b) highlights the variation in FF and efficiency with increased in temperature. The FF is increased from ~74.6 to ~77.9 till 280 K as temperature increased. After that FF decline progressively, to ~74.8 at 340 k, due to enhanced non-radiative recombination and interfacial losses at elevated temperature. The efficiency shows a slightly different trend, it rises form ~17 to ~18.3 at 300 K. However, with further increased in temperature, efficiency decreased gradually reaching ~16.9 at 340 K, primarily due to the combined reduction in FF and Voc. This analysis confirms that while moderate heating (280-300 K) enhances device performance by supporting carrier mobility and lowering resistive losses, excessive temperature (> 320 K) significantly degrades photovoltaic efficiency through enhanced recombination and thermal instability at the interfaces.

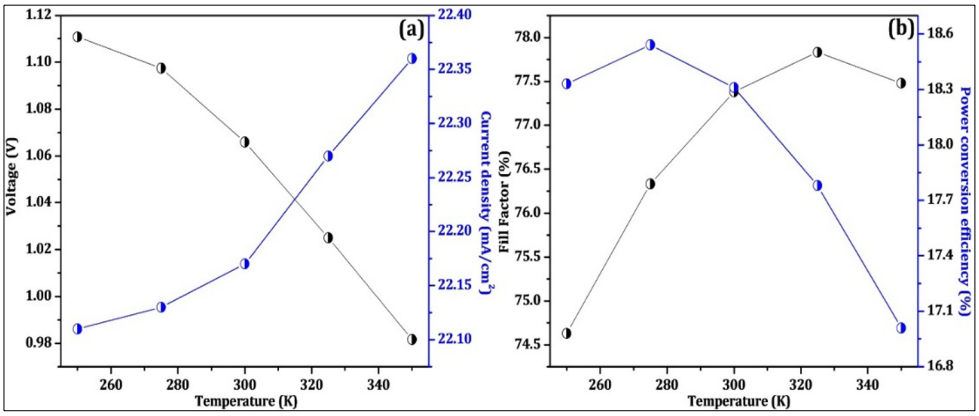

Fig. 6. (a) Depicts difference of Voc and Jsc with temperature and, (b) Effect of temperature on FF and PCE, with peak performance near 300 K.

In addition to increased carrier recombination, inherent thermal breakdown mechanisms in perovskite absorber layer are also responsible for the temperature dependent drop in Voc and PCE. By causing lattice expansion and ion migration, especially of I^- and MA^+ ions, towards the ETL and HTL interface, elevated temperature produces interfacial defect states and promotes non-radiative recombination. Furthermore, partial phase transitions or lattice deformation or lattice deformation within $MAPbI_3$ can result from thermal stress, which further reduces carrier lifetimes.

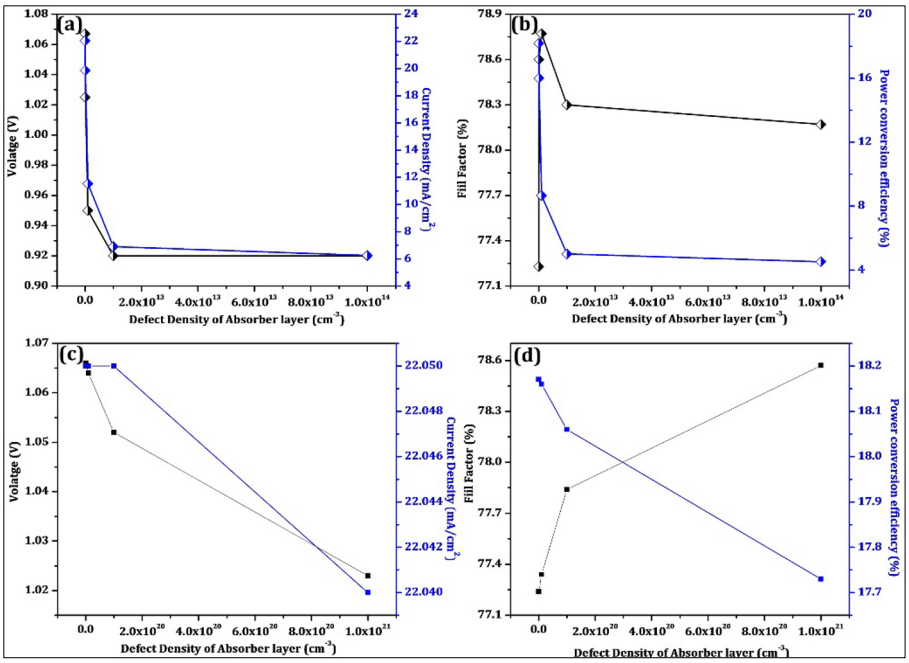

Fig. 7. (a) Depicts the influence of interface defect density on the photovoltaic parameters (a) Voc and Jsc for ETL/absorber interface and (b) FF and PCE for ETL/absorber interface, (c) Voc and Jsc for HTL/absorber interface, and (d) FF and PCE for HTL/absorber interface.

The observed behaviour is physically compatible with known deterioration mechanisms: the simulated temperature coefficient of Voc. A sensitivity study on interface defect densities was carried out by altering the defects states at the PAL/HTL and ETL/PAL interfaces from 1 x 10^{10} to 1 x 10^{14} cm^{-2} in order to better evaluate the influence of interfacial quality on device performance. Figure 7 (a-d) indicates that whereas Jsc varies only little, the Voc and fill factor decrease quickly as interface defect density increases. Higher defect density boost non-radiative recombination losses at the interface, as seen by the efficiency considerable decreased. For PSCs to achieve high and consistent PCE interface passivation must be improved and defect formation must be reduced. At elevated temperature, lattice vibrations may increase and promote carrier dispersion and defect assisted recombination. This lowers the Voc by increasing non-radiative losses and decreasing quasi-fermi level splitting. Also, recombination is accelerated by the rise in intrinsic carrier concentration at higher temperatures, which lowers device overall performance.

Conclusion

In this study, SCAPS-1D simulations tool were engaged to explore the effect of PAL thickness and working temperature on the performance of designed PSCs with the device architecture FTO/α-Fe_2O_3/$MAPbI_3$/Spiro-OMeTAD/Au. The ideal device with the optimal thickness of ~600 nm reveals the notable efficiency of ~18.3%. It achieves a J_{SC} of ~22.1 mA/cm^2, a V_{OC} of ~1.06 V, and a FF of ~77.4 %. The Temperature dependent study reveals the thermal sensitivity of α-Fe_2O_3 based ETL. The FF increased from ~74.6 % at 250 K to a peak of ~ 77.9 % at 280 K, then declines to ~74.8 % at 350 K due to improved non-radiative recombination and interfacial losses. Similarly, the efficiency increases from ~17.0 % at 250 K to ~ 18.3 % at room temperature, after that decreased sharply to ~16.9 % at 350 K. Generally, these findings found that the ideal device structure achieves its optimal performance near room temperature and at a PAL of 600 nm. Beyond these limits, device efficiency and stability are compromised, underlining the need for careful structural and thermal management in the design of α-Fe_2O_3 based PSCs. This study reflects that α-Fe_2O_3 affords a scalable and thermally stable ETL alternative allowing for Long-lasting PSCs topologies that are appropriate for large area manufacturing and long term operational dependability.

References

1. M. Kumari, M. Kaur, A.K. Tangra, Numerical optimization of HTL-free perovskite solar cells: a pathway to enhanced efficiency. ICCK Transactions on Advanced Functional Materials and Processing **1**, 25–31 (2025). https://doi.org/10.62762/TAFMP.2025.303826
2. U. Mandadapu, S.V. Vedanayakam, K. Thyagarajan, M.R. Reddy, B.J. Babu, Design and simulation of high efficiency tin halide perovskite solar cell. Int. J. Renew. Energy Res. **7**, 1603–1612 (2017).
3. G.S. Lotey, N.X. Sun, A.K. Tangra, M.B. Kanoun, S. Goumri-Said, A.A. Kanoun, A. Tovstolytkin, J. Kaur, M.P. Garg, Boosting efficiency and stability of perovskite solar cells via integrating engineered Li/Na-ferrite-based inorganic charge transport layers: a combined experimental and theoretical study. J. Nanopart. Res. **25**, 179 (2023). https://doi.org/10.1007/s11051-023-05827-x
4. M. Rahman, S. Miah, S. Marma, M.S.W. T. Sabrina, Simulation-based investigation of inverted planar perovskite solar cell with all metal oxide inorganic transport layers. In 2019 International Conference on Electrical, Computer and Communication

Engineering (ECCE), IEEE, 1–6 (2019). https://doi.org/10.1109/ECACE.2019.8679283

5. I.J. Ogundana, S.Y. Foo, Improving the morphology of the perovskite absorber layer in hybrid organic/inorganic halide perovskite MAPbI3 solar cells. J. Solar Energy **1**, 8549847 (2017). https://doi.org/10.1155/2017/8549847
6. F. Izadi, A. Ghobadi, A. Gharaati, M. Minbashi, A. Hajjiah, Effect of interface defects on high efficient perovskite solar cells. Optik **227**, 166061 (2021). https://doi.org/10.1016/j.ijleo.2020.166061
7. C.W. Chang, Z.W. Kwang, T.Y. Hsieh, T.C. Wei, S.Y. Lu, High performance perovskite solar cells fabricated from porous PbI2-xBrx prepared with mixture solvent pore generation treatment. Electrochim. Acta **292**, 399–406 (2018). https://doi.org/10.1016/j.electacta.2018.09.161
8. M. Rai, L.H. Wong, L. Etgar, Effect of perovskite thickness on electroluminescence and solar cell conversion efficiency. J. Phys. Chem. Lett. **11**, 8189–8194 (2020). https://doi.org/10.1021/acs.jpclett.0c02363
9. A. Sławek, Z. Starowicz, M. Lipiński, The influence of the thickness of compact TiO2 electron transport layer on the performance of planar CH3NH3PbI3 perovskite solar cells. Mater. **14**, 3295 (2021). https://doi.org/10.3390/ma14123295
10. A. Kumar, S.K. Ojha, N. Vyas, A.K. Ojha, Designing organic electron transport materials for stable and efficient performance of perovskite solar cells: a theoretical study. ACS Omega **6**, 7086–7093 (2021). https://doi.org/10.1021/acsomega.1c00062
11. C. Tang, B. Sun, M. Li, J. Zhang, X. Fan, F. Gao, Y. Tong, L. Dong, Y. Li, Surface hydroxylated hematite promotes photoinduced hole transfer for water oxidation. J. Mater. Chem. A **7**, 8050–8054 (2019). https://doi.org/10.1039/C9TA00561G
12. Y. Kumar, R. Kumar, P. Raizada, A.A.P. Khan, A. Singh, Q.V. Le, P. Singh, Current status of hematite (α-Fe2O3)-based Z-scheme photocatalytic systems for environmental and energy applications. J. Environ. Chem. Eng. **10,** 107427 (2022). https://doi.org/10.1016/j.jece.2022.107427
13. L. Lin, T.W. Jones, T.C.J. Yang, N.W. Duffy, J. Li, L. Zhao, G.J. Wilson, Inorganic electron transport materials in perovskite solar cells. Adv. Funct. Mater. **31**, 2008300 (2021).
14. M.S. Bakshi, Iron oxide nanomaterials at interfaces for sustainable environmental applications. Acc. Mater. Res. **5,** 1000–1012 (2024). https://doi.org/10.1021/accountsmr.4c00151
15. G.A. Waychunas, C.S. Kim, J.F. Banfield, Nanoparticulate iron oxide minerals in soils and sediments: unique properties and contaminant scavenging mechanisms. J. Nanopart. Res. **7**, 409–433 (2005). https://doi.org/10.1007/s11051-005-6931-x